Cross sections of exotic light nuclei

Master's thesis, 7.10.2019

Author:

Jussi Louko

Supervisor:

Wladyslaw Trzaska

UNIVERSITY OF JYVÄSKYLÄ
DEPARTMENT OF PHYSICS

Abstract

Louko, Jussi
Cross sections of exotic light nuclei
Master's thesis
Department of Physics, University of Jyväskylä, 2019, 51 pages.

Cross sections for ^{6}He, $^{7-9}$Li, $^{10-12}$Be and ^{14}B nuclei on ^{28}Si, ^{181}Ta and ^{59}Co targets were measured at 10 – 60 MeV u^{-1} energy range using modified transmission method. In total, 120 cross sections were extracted. The purpose of the experiment was to investigate an unexpected behavior of cross sections found in certain exotic nuclei. Especially of interest was a sudden growth, observed in heavy helium and lithium isotopes at low energies. These features are presumably manifestations of a halo and cluster-like structures in these nuclei. Obtained results may yield relevant data for the development of more accurate microscopic nuclear models and radiation resistant electronics. In this work, a detailed description is given of the measuring setup and the methods used in the experiment.

Keywords: exotic nuclei, total reaction cross section, cross section, halo, neutron halo, proton halo, cluster

Tiivistelmä

Louko, Jussi
Keveiden eksoottisten ytimien kokonaisvaikutusalojen mittaus
Pro gradu-tutkielma
Fysiikan laitos, Jyväskylän yliopisto, 2019, 51 sivua

Tässä pro gradu-tutkielmassa perehdytään kokeeseen, jossa eksoottisten ^{6}He, $^{7-9}$Li, $^{10-12}$Be ja ^{14}B ytimien vaikutusaloja ^{28}Si, ^{181}Ta ja ^{59}Co kohtioihin, mitattiin 10–60 MeV u^{-1} alueella. Tutkimuksen tavoitteena oli kerätä lisää dataa aiemmin havaituista poikkeavuuksista, näiden ytimien kokonaisvaikutusaloissa. Erityisesti mielenkiinnon kohteena olivat äkillisesti pienillä energioilla kohoavat vaikutusalat, tietyissä eksoottisissa helium ja litium ytimissä. Nämä poikkeamat ovat oletettavasti ytimien haloja klusteri-rakenteiden seurausta. Tuloksia voidaan käyttää tarkempien mikroskooppisten ydinmallien kehittämisessä. Lisäksi niitä on mahdollista hyödyntää uusien ja paremmin säteilyä kestävien puolijohteiden suunnittelussa. Tutkielman pääpainona on käytetty koeasetelma ja analyysimenetelmät.

Avainsanat: eksoottiset ytimet, kokonaisvaikutusala, vaikutusala, halo, neutroni halo, protoni halo, klusteri

Preface

The work presented in this thesis was carried out at the Flerov Laboratory of Nuclear Reactions in JINR, Dubna during March 2019.

First, I would like thank my supervisor Wladek, who initiated this collaboration and made this opportunity possible for me. I would like to thank all the people who have participated in the experiment and helped with the measurements. Especially, I would like to say thanks to Yuri Sobolev, who generously invited me to Dubna to participate in the experiment. Big thanks to Sergey, Ivan and Talgat also, for taking care of me during the experiment and showing some local customs to me. Thanks to Vladimir Maslov for the help with the data analysis. Thanks to the head of department, Yuri Penionzhkevich, for the hospitality during my visit.

This has been a wonderful experience for me and I hope that I have been at least some help during the experiment and our collaboration continues in the future as well.

Jyväskylä, October 2019

Jussi Louko

List of abbreviations

IAEA	International Atomic Energy Agency
CEM	Cascade excitation model
TOF	Time-of-flight
CsI(Tl)	Thallium activated Cesium Iodide (scintillation detector)
AC-detector	Active collimator detector
dE-detector	energy loss (silicon) detector
$CeBr_3$	Cerium bromide (scintillation detector)
ADC	Analog to digital converter
PMT	Photo multiplier tube
NIM	Nuclear Instrument Module
CAMAC	Computer aided measurement and control
TFA	Timing filter amplifier
CFD	Constant fraction discriminator
TDC	Time to digital converter
LAM	Look-at-me

Contents

1 Introduction

This work describes a new setup and data analysis methods used to investigate anomalies in the total reaction cross sections of exotic nuclei. This experiment is the latest, in a series of measurements that started in the early 2010s. Since then, multiple experiments have been successfully carried out. Each experiment had a more advanced setup and a slightly different goal. The experiments were primarily focused on studying the total reaction cross sections of different helium and lithium isotopes on silicon targets [1]–[5].

An peer reviewed paper will be published about this experiment later on. In it, the results and theoretical analysis will be discussed in more formal manner. Consequently, this thesis will be a more practically orientated and focuses more on the technical side of the things.

In this work, the actual physical implementation of the experimental setup will be discussed in a detail. More accurate description about the methods and computer programs used is given. The shortcomings of the setup, along with other, mostly practical, difficulties encountered during the measurements is discussed. Possible improvements for the future experiments is also being looked at.

1.1 Exotic nuclei and halos

A.I. Baz predicted the existence of nuclear states possessing enhanced radii already in the 1959 [6]. These states would remain purely speculative for almost thirty years. In 1985, the first concrete evidence of such enlarged nuclear state was made by I. Tanihata et al. [7]. Two years later in 1987, another new discovery was made by P. G. Hansen and B. Jonson, which confirmed the existence of dilute surface region in some neutron-rich light nuclei, close to the drip line [8].

The states had a two-body structure, a core with normal nuclear density and dilute surface region containing only valence nucleons. This region would make them much larger than their stable counterparts. States possessing this new feature, became to known as a halo states and the nuclei possessing them, were called exotic nuclei. Later on, the term exotic nuclei was extended to all nuclei, lying near the nucleon drip lines.

The physical reason of this effect is the weak binding energy between the valence neutrons and the core. This leads to long “tails” in the wave function. The effect is

expected to be especially prominent for the neutrons occupying the s-orbit, because of the absence of centrifugal barrier [9].

Among the most spectacular examples of such nuclei is the one-neutron-halo isotope ^{11}Be. In its ground state, the average distance between valence neutron and the center of the nuclear core (halo radius or charge radius) can reach up to 8 fm, size comparable to that of an uranium nucleus [10]–[12].

At first, these states were believed to only exist in the ground states of nuclei, lying near the drip lines. However, soon it became evident that this phenomenon was not limited only to the unstable exotic nuclei, but instead, they could be found in large numbers on excited states of nuclei, on and off the β-stability line.

In addition to the one nucleon halos, a more complex halo states composed of two or even four nucleons were found. These new discoveries challenged existing nuclear models at the time, as their existence was not predicted correctly or at all.

Nevertheless, as more and more of these exotic states, possessing halo-like structures and properties began to be found, a need for more precise and rigorous definition became inescapable [10], [13]–[21].

In papers by K. Riisager and A. S. Jensen et al., the halo state was characterized by two distinct features: a large probability of a cluster component in the total wave function and a large spatial extension, meaning that more than half of the probability should be in the forbidden region, outside the classical turning point [22], [23].

However, it should be kept in mind that only a handful of these halo states have been discovered. New studies are constantly revealing more and more exotic states possessing new and unprecedented properties, so the exact definition and the requirements are still evolving.

One thing is for sure though, exotic nuclei will continue to be one of the key areas to study for nuclear physicists around the world for a long time. They will test our theories and challenge our understanding about the deepest nature of nuclear physics.

2 Motivation

One of the most fundamental and important features of a nucleus is its radius. It reflects the properties of both nucleon–nucleon interaction and nuclear matter. The radius plays a key role in all nuclear physics, with a result that even its modest deviation from the standard values may cause radical changes to the nuclear structure and properties.

Exotic light nuclei are particularly interesting, because they provide a very special case, where we can more easily test and improve our microscopic nuclear models and shed light to the mysteries of the galactic evolution.

2.1 Why use light nuclei and why they matter

Experimenting with light nuclei is beneficial due to their small proton and neutron numbers. Even if only few nucleons are added or removed from the light nuclei, their N/Z values will change significantly and they may undergo transitions from ordinary states to exotic halo states. For example, isotopes of helium go through N/Z values, all the way from 0.5 to 4.0. The same is not true for heavy elements, as they have much more nucleons and the N/Z ratio is not as susceptible to changes.

Light nuclei also have an added benefit of being much easier to produce and handle in experiments compared to heavy nuclei, due to their low masses and smaller energies required.

The size of the nuclei, and thus the halo states, are directly linked to the reaction cross section, which is the key property in many processes across the universe. Exotic states of ^{12}C, for example, play a very important role in helium and carbon burning processes inside massive stars, which are responsible for the existence of elements, heavier than helium, in our universe. Exotic states are also thought to have an important role in the r-process and in formation of elements heavier than iron, which are produced in the most extreme astrophysical phenomena such as supernovae or colliding and merging neutron stars [24].

This is not to say that the heavy elements are not as interesting as the light nuclei. Exotic heavy nuclei may not be as important in the stellar nucleosynthesis, but they have totally different set of unique properties due to their large size and masses. Studying heavy elements has its time and place, but using light nuclei is often expensive and less demanding from the experimental point of view.

2.2 Practical applications

Developing and understanding the fundamental mechanics of nuclear reactions is something to strive for, especially from point of view of basic research, but studying and measuring the reaction cross sections has plenty of practical uses as well.

Some of these applications include, various space related issues such as astronaut radiation dosage, electronics malfunction analysis, structural materials analysis and galactic cosmic rays shielding. Medical applications include, hadron therapy for cancer, radiation shielding, medical isotope production and high-radiation environment dosimetry. Environmental applications include, for example, transmutation of nuclear waste.

The most direct consequence of this study, will be the new cross sectional data, which may be useful for designing radiation hard electronics for space applications. Other, perhaps more research oriented applications, include accelerator design, rare isotope production, neutron sources for condensed matter physics and simulation of detector set-ups [25].

What all of these applications have in common is that they rely on computing tools, developed for the simulation of spallation reactions. Especially, more accurate cross sectional data could be used to improve the cascade excitation models (CEMs). Simulations use these to compute the production yields and characteristics of all the particles and nuclei generated in various nuclear interactions.

Currently the CEMs rely on old cross sectional measurements and their predictions are found to be inaccurate. The 2008-2010 international atomic energy agency (IAEA) Benchmark of Spallation Models suggested that the CEMs should be improved to get better predictions for the production of energetic light fragments in particular [26].

3 Experiment

Experiment studying the energy dependence of total reaction cross sections for ^{6}He, $^{7-9}$Li, $^{10-12}$Be, ^{14}B nuclei on ^{28}Si, ^{181}Ta, ^{59}Co targets in the energy range of 10 – 60 MeV u^{-1} was carried out at Flerov laboratory of nuclear reactions, JINR, Dubna in March 2019. The measurements were done on a channel of the achromatic fragment separator ACCULINNA of the U-400M cyclotron [27], [28].

The experiment was a continuation in series of measurements, investigating an interesting enhancement of the total cross sections in some neutron rich isotopes. Of particular interest were certain helium and lithium isotopes, on which the excess in the cross sections was observed at the energy ranges of 20 – 30 MeV u^{-1}, during the previous experiments [3], [5]. This phenomenon is thought to be caused by the weakly bound nucleons and the resulting cluster structures in these exotic isotopes.

3.1 Overview and basic principle

The total reaction cross sections were extracted using modified transmission method. This method is based on measuring the reaction products, as opposed to the attenuation method, in which the relative attenuation of the beam is being measured, after the target, as seen in figure 1. In theory, measuring the total reaction cross section using the modified transmission method is very straightforward. All you need to do is to measure how many nuclear interactions occur for given incident particle flux.

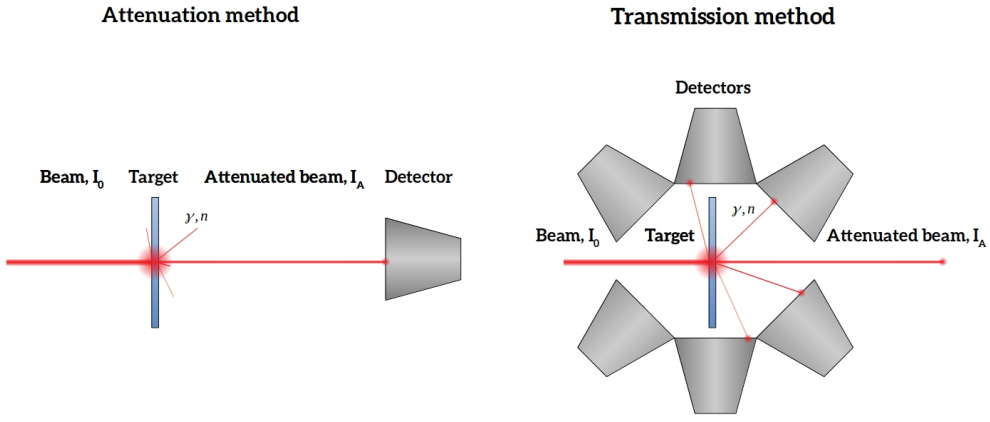

Figure 1. Two different methods to measure total reaction cross sections. No technique is vastly better than the other. They both have their problems, particle identification and background noise to name a few.

However, in practice, this is easier said than done. It is not always very clear, when a projectile has interacted with the target nucleus. Moreover, the harsh reality is that with real physical setup and detectors, there are bound to be uncertainties from a wide range of different error sources. These include things such as imperfect electronics, spectroscopic parameters and background noise. All these things have to be taken into a consideration, when building the setup and analyzing the results.

To tackle these problems, careful planning was needed. Using the experience obtained from the preceding experiments, new improved setup was constructed. Excluding the accelerator and separator, the new experimental setup consisted of two distinct sections.

The first part of the setup was a multi-layer detector telescope, whose primary purpose was to identify and track the incoming particles. This was necessary, because the beam was made up from various different isotopes. The use of impure beam was deliberate and it was done so that multiple cross sections could be measured simultaneously, saving a lot of time. It also greatly simplified the production of the exotic nuclei, as extremely pure beam was not needed.

The second part of the setup was a cylindrical spectrometer, which was used to detect the prompt gamma particles and neutrons, originating from the interactions between the projectile and target nuclei. The beam was produced in such a way that the projectiles had wide angular momentum distribution when populating the reaction channels, which translated in a rather broad distribution over the momentum. For this reason, the spectrometer had to have an efficiency close to 100% across all gamma multiplicities and energies for accurate and reliable results.

One of the most essential parts of the setup, besides the spectrometer, was the main dE-detector of the telescope. It provided the trigger signal for opening the normally closed ADCs and TDCs and started the data acquisition process. In other words, it determined which events were accepted and thus the input flux of the setup. It also provided the necessary energy loss data for the particle identification and collision energy calculations.

The total reaction cross sections were finally calculated from the collected data using a linear approximation for thin film targets normalized to the background. More detailed description of the setup, analyzing methods used and how the measurements were carried out is given in the following sections. Extra pictures and figures can be found on appendix D.

3.2 Beam and separation

Primary beam of $^{15}N^{+7}$-ions, from the U-400M cyclotron was accelerated to 49.7 MeV u^{-1} or 745 MeV total was focused onto 500 µm thick beryllium production target. The production target was located at the object plane of the ACCULINNA beam channel, marked F1 in the figure 2.

Resulting secondary beam contained multiple different light nuclei and their isotopes. Most of these were unwanted, ordinary nuclei and further purification was needed to separate the beam into a mix of interesting exotic isotopes. The Separation was done based on the different mass-charge ratios of the isotopes using the ACCULINNA achromatic magnetic separator. Combination of neutron heavy isotopes of helium, lithium, beryllium and boron was achieved at the second focus.

Ion optics configuration and simplified schematic of the ACCULINNA separator are shown in figure 2. Tuning the yields for different projectile isotopes was done almost exclusively by adjusting the electric currents in the two main separation dipole magnets D1 and D2. Only minor adjustments had to be done with the focusing quadrupole magnets Q1 – Q15.

The total energy of the beam could be done by adjusting the magnetic elements of the separator. At higher energies this could be done without significant loss of the intensity. However, at lower energies, replaceable polyethylene plates had to be used and, depending on the thickness of the plates (0 – 5 mm), some intensity was lost.

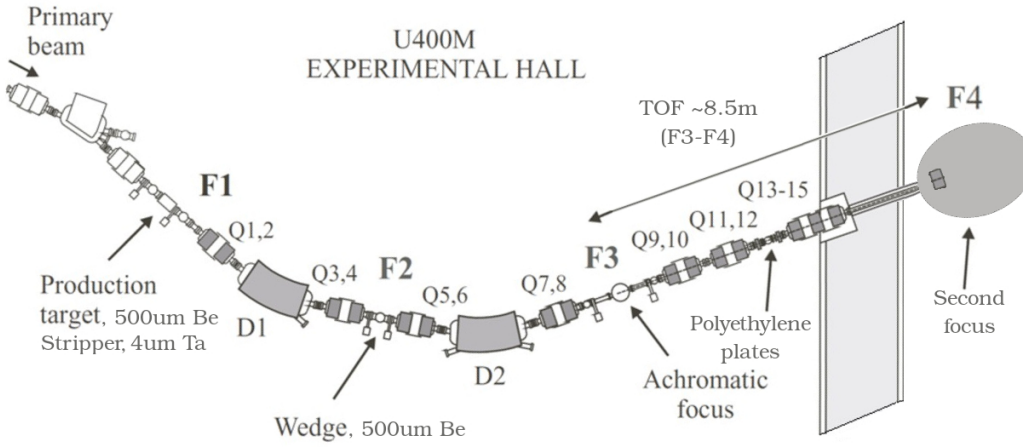

Figure 2. Schematic of the ACCULINNA separator. F1 – the object plane; F2 – the intermediate dispersion plane; F3 – the achromatic focal plane; F4 – the second focal plane; D1-2 dipole magnets; Q1-15 quadrupole magnets.

The experimental setup, all the way from the object plane of the separator to the target plane, was modeled and simulated using LISE++ program [29]. The simulation provided estimations for the optimal separator parameters for getting the maximum yield of desired isotopes to the focusing plane (Fig. 3a). Without the simulation, finding the best parameters would have been completely guesswork and taken much longer. The simulation was also used to help with the identification of the particles and sanity checking the results (Fig. 3b) as well as to calculate the collision energies at the target plane (see section 4.3).

It is clear that the LISE++ is a very useful tool for any experiment involving nuclear interactions. It was developed for the needs of nuclear spectroscopy groups and it can calculate the transmission and yields of fragments produced and collected in a arbitrary spectroscopic setups. It is easy to use and it can be used to simulate and test new experimental setups before they are being build.

LISE++ offers multiple powerful simulations, such as an Monte Carlo simulation of fragment transmission, Monte Carlo simulation of fission fragment kinematics and ion optics calculation and optimization. In addition, it has handy collection small applications for calculating and visualizing things, for example, it can plot energy loss, time-of-flight, position, angular, charge and cross section distribution and dE-E, dE-TOF, Z-A/Q and dE-X two-dimensional plots of a simulated setup.

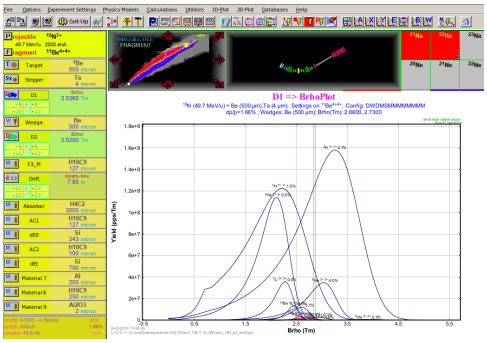

(a) Screen capture of the LISE++ simulation. The simulation was used to optimize the D1 dipole magnet, so that maximum yield of interesting isotopes were achieved at the focusing plane of the setup.

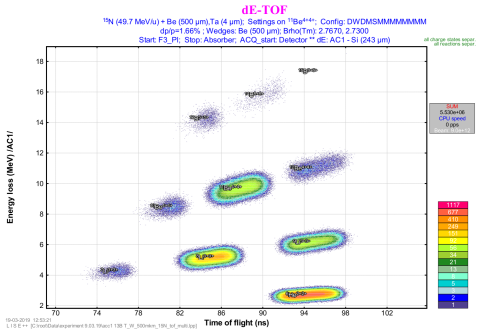

(b) Simulation of the dE-TOF graph using LISE++ program's Monte Carlo function. The simulation could be used, for example, to troubleshoot and identify the different isotope peaks during the experiment.

Figure 3. LISE++ simulations were used to help with the measurements. The simulations were utilized throughout the experiment with very good results.

3.3 Detector setup

Measuring the total reaction cross section with the transmission method requires accurate registering of the incident particles and their possible reaction gammas. In this experiment, a total of 16 detectors were used, resulting in 32 channels.

Slightly different approach was taken in this experiment, compared to the prior experiments, in efforts to suppress the background noise. Detailed description of the previous setups and experiments can be found on references [1]–[5].

The detector setup used in this experiment was as follows: two 127 µm thick plastic ($H_{10}C_9$) scintillation detectors for measuring the time of flight of the incoming particles, one 243 µm thick silicon detector for measuring the energy loss of the particles and for generating the primary start trigger of the setup. One more plastic scintillation detector, 100 µm thick, for creating the collimation condition for the beam. And lastly, twelve hexagonal CsI(Tl) based scintillation detectors (150 mm long, 100 mm outer radius), arranged to cylindrical formation (87 mm apart), for detecting the possible reaction gammas of the incident particles. CsI(Tl)-detectors were accompanied with traditional PMTs and their inner sides were covered with light reflectors and shield. The outer sides were additionally covered with 1 mm thick Cd, Pb and Cu foils.

The start detector for the time-of-flight measurement was located at the achromatic focal plane of the ACCULINNA separator and the stop detector was placed just before the second focal plane. Straight flight path between these detectors was roughly 8.5 meters. The time resolution achieved with this TOF setup was around 140 ps. The energy reducing plastic plates were situated halfway between the TOF detectors (Fig. 2 and Fig. 4).

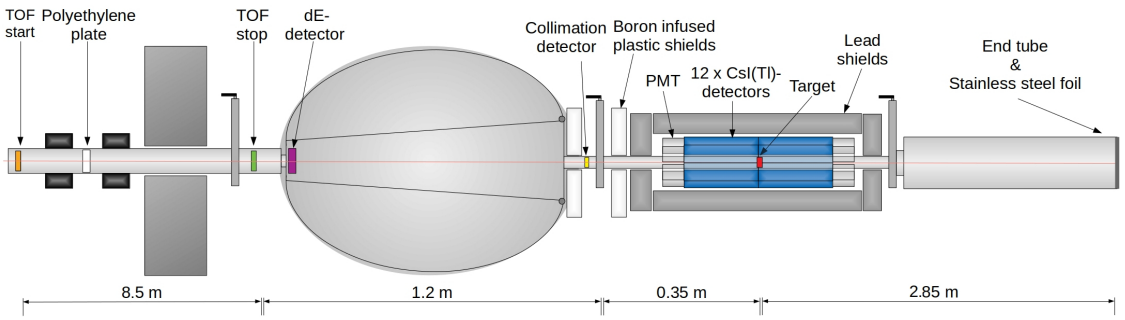

Figure 4. Schematic of the setup. Not in scale.

After the beam passed through the TOF system and exited the separator, it hit the primary dE-detector. The dE-detector was placed at the entry of a larger vacuum chamber. Different elements and isotopes deposited a specific portion of their total kinetic energies to this detector. In this experiment, a passive target was used and as a result, there was no way to directly measure the energy of the particles at the target plane. To get around this problem, LISE++ simulations had be used to indirectly estimate the average collision energies, based on the energy losses at the dE-detector. More about that in section 4.3.

The energy loss data and the time of flight data could be then plotted together as a two dimensional graph, where separate isotopes formed distinct peaks, allowing accurate identification of the incoming particles.

Next detector in the sequence was the active collimation scintillation detector. It created, together with the stop detector of the TOF system, a collimation condition for the incoming particles. This was done to cut out the false triggers from particles that may have been dispersed from the other detectors or otherwise going to miss the target. If there was a event in the stop detector and shortly after, another one in the AC-detector, it was concluded that a particle was heading straight towards the target and it was accepted in the data analysis.

All detectors thus far, have been strictly for identifying and tagging the incoming particles and their energies. Next, the particles hit the actual target, which was either a thin cobalt (65 µm), silicon (790 µm) or tantalum (110 µm) film (Fig. 5).

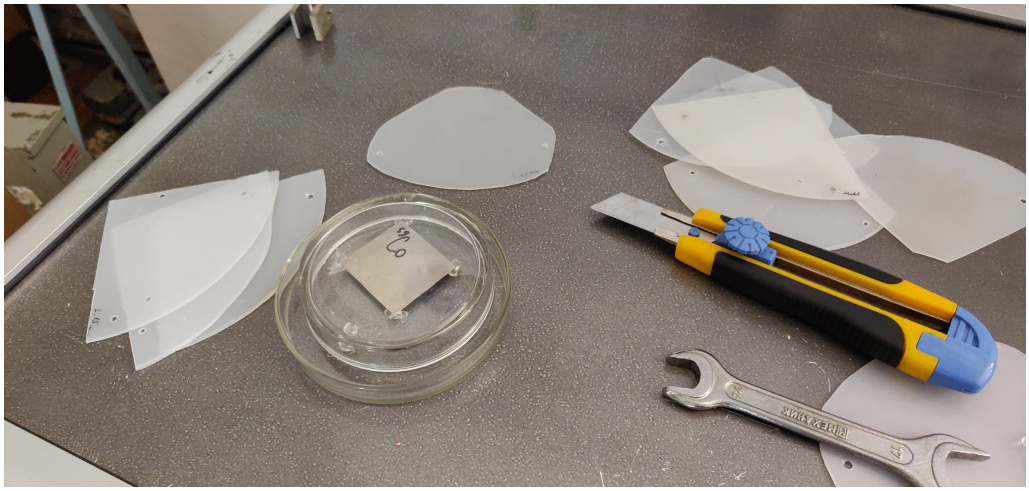

Figure 5. Cobalt target and some of polyethylene plates, which were used to adjust the collision energies in low ranges.

The second part of the transmission method required accurately detecting how many of the tagged projectile particles interacted with the target nuclei. Vast majority of these nuclear reactions would emit an gamma particle or a neutron, which could be detected. For this, the setup used twelve CsI(Tl) scintillation detectors, arranged as a cylindrical 4π-γ-spectrometer formation around the target.

The array was shielded from background with 5 cm thick lead bricks and boron loaded polyethylen plates. These shields were strategically placed to protect the spectrometer from the outside influence, but also from the background events, originating from within the setup. Such events could be, for example, stray particles dispersed by the AC-detector (Fig. 6).

However, despite all this shielding, enough background was still getting in to skew the results. For this reason, an additional background measurement was required. These background measurements were done without the target, to get an accurate baseline for the background. The results from these runs were then used to evaluate the false readings from the real ones by using a statistical normalization method.

After the target, the remaining beam continued into 2.0 m long steel tube, with larger diameter and 110 µm thick stainless steel foil at the end. This was done to eliminate as much of the reflections and noise from the leftover beam as possible.

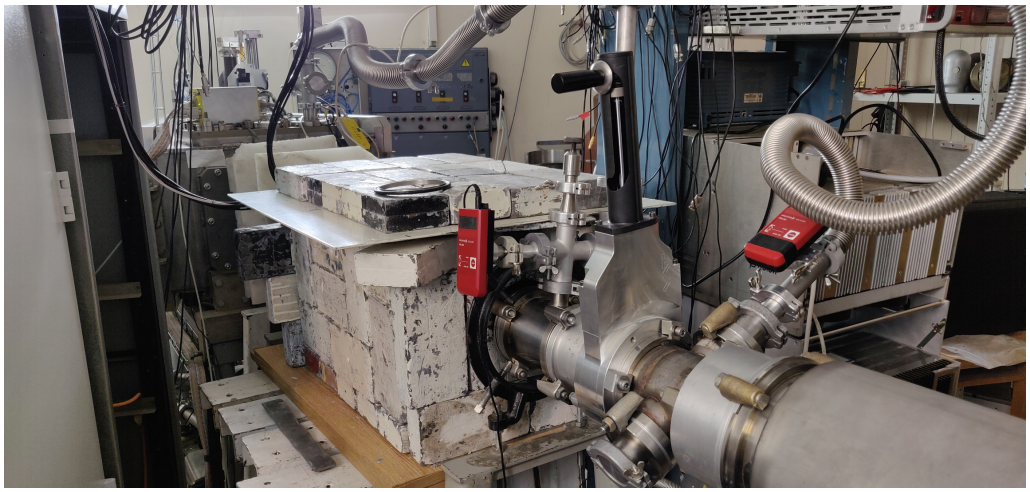

Figure 6. Overview of the actual measuring setup. The spectrometer (in the middle) was shielded with 5 cm thick lead bricks and 10 cm boron loaded polyethylen blocks for minimizing the background quanta. The system was kept around 10^{-5} mbar throughout the whole experiment and the vacuum had to be broken only briefly, in a small section of the setup, for target change.

3.4 Electronics and data acquisition

Relatively low beam intensity was used during the measurements, mainly to avoid pulse pile up in the telescope and limit the dead time of the slow CsI(Tl) scintillators and associated electronics. The count rate at the dE-detector was kept around 100 – 1000 Hz, depending on the target thickness and beam energy

Electronics and data acquisition setup was fairly standard. It was implemented using NIM and CAMAC modules. Block diagram for all essential parts of the experimental setup is presented in figure 7. Precise make and model numbers of equipment used are listed on appendix, part B.

The first portion of the telescope setup was for measuring the time-of-flight of the incoming particles. Only the time signals from these two DC-biased plastic scintillation detectors were needed. The time signals from the preamlifiers, were further amplified and shaped using timing filter amplifiers and digitized with constant fraction discriminators in preparation for the time-to-amplitude converters. Signals from these TACs were read and hold with peak sensing ADCs. Similar setup was used for the time signals of the AC-detector.

Signal processing for the spectrometer's signals were little more complex, since its photomultipliers had fast rise times. 16 channel combination unit, which implemented programmable shaping / timing filter amplifiers, CFDs and multiplicity triggers for each channel was used. Output generated separated and ready to go energy and time signals, which were subsequently fed into time-to-digital converters and peak ADCs.

Similar set of electronics was used for the dE-detector, which generated the main start signal for the setup as seen on the figure 7. It also provided the start signal for the TACs of the spectrometer's TDCs.

In addition, this time signal was also used for monitoring the beam intensity. Arduino UNO based system was used to count the pulses and it was set up to make an Skype call to person in charge, if the beam was being unstable. This monitoring system was designed and constructed by the author. More detailed description can be found in section 3.5.

The digitized main start signal from the dE-detector, signaled the master trigger unit, which enabled all the ADCs and TDC for 4 µs, determined by the characteristics of the slow CsI(Tl) scintillation amplifiers. Upon completing data collections and the analog-digital conversions, the CAMAC crate controller read the buffers and send them to the PC for recording events in each buffer. Once the data were saved, the

ADCs and TDCs were cleared by CAMAC commands in preparation for the next event. During setting up of the system, each signal was checked with an oscilloscope and matched to the gate signals by adding delay lines when needed.

Arranging the data acquisition this way had its advantages and disadvantages. Reading all the buffers even though the sources may have been floating at the time of reading caused false readings on these channels and one had to be careful when processing the raw data. The biggest benefit of this method was the wide range of post-processing options, due to additional information about the multiplicities and geometric distributions of the events.

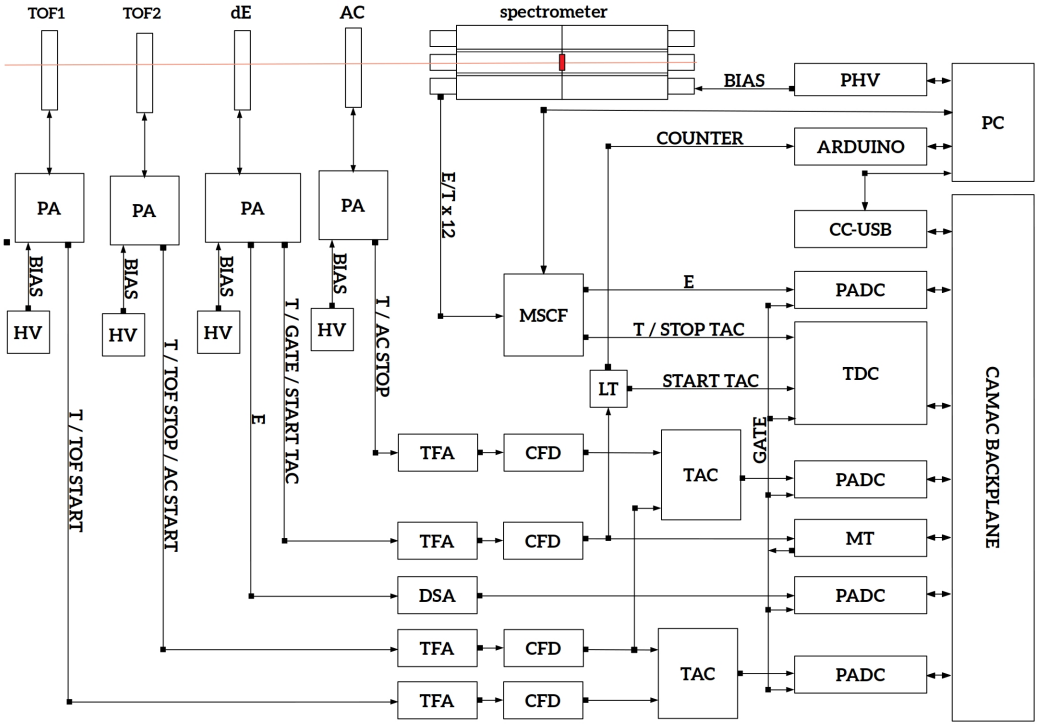

Figure 7. Block diagram of the setup. For simplicity, some elements, such as delay lines, FIFOS, gate generators and LTs have been left out. (PA) preamplifier, (HV) high-voltage supply, (PHV) programmable high-voltage supply, (DSA) spectroscopy amplifier, (TFA) Timing filter amplifier, (CFD) constant fraction discriminator, (MSCF) Programmable shaping / timing filter amplifier with LEDs and multiplicity trigger, (TDC) time-to-digital converter, (TAC) time-to-amplitude converter, (PADC) peak sensing AD converter, (MT) master trigger, (LT) Logic level transformer and (CC-USB) CAMAC crate controller.

3.5 Monitoring the beam using Arduino UNO

Should there be any problems with the cyclotron, stability of the beam had to be monitored throughout the 12-hour-long measurement runs. Previously, CAEN scaler, which had only a seven segment display for output was used. An IP-camera was used to manually check the counts on the scaler every now and then. It was quickly discovered that this was somewhat unreliable and also a very tedious job, especially during the night times. A better solution was clearly needed, and with equipment at hand, an Arduino UNO based counter was quickly put together by the author.

In these low intensity measurements, Arduino's 200 kHz counting capability was more than adequate. First, the $-0.7\,\mathrm{V}$ digital NIM pulses from the dE-detector had to be converted into Arduino compatible $5\,\mathrm{V}$ logic using a level translator. A short code, which was counting the pulses on one of the digital input pins and sending the readings through the serial port to the PC, was uploaded to the Arduino. On the PC, a small JAVA program was written in order to communicate with the Arduino and to provide a user interface and layer to interact with Skype (Fig. 8).

In the program, upper and lower thresholds for the count rate of the dE-detector could be set. The program showed the count rate in real time and also an average counts over a set time interval. The averaging was done, so that short and small fluctuations of the beam would not trigger the alerter. A timeout after an alert could be set so that cyclotron operator had time to stabilize the beam before the next alert. Persons in charge of the monitoring would install Skype to their mobile phones and if a problem was detected, the program would alert them by calling them.

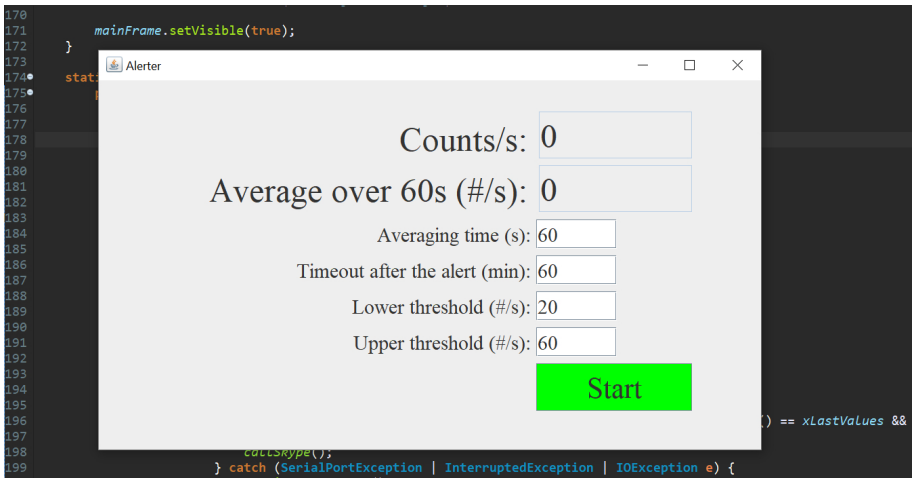

Figure 8. GUI of the alerter program.

4 Data analysis

The data analysis was mostly done with CERN's ROOT toolkit [30]. Couple other programs were used for managing and presenting the data. In total, 34 measurement runs were done, two of which were calibration runs for the spectrometer and the dE-detector. Around 700 hours of beam time was used and approximately 100 gigabytes of raw binary data was collected throughout the experiment. To get consistent data across all the measurement runs, changes between each run were kept minimal and they all followed same order of operations.

First, the baseline background was measured at certain energy, without the target. Then, while keeping all other settings unchanged, the chamber was opened and the first of the three targets was placed in. After enough statistics were collected with each target, a new energy and optimized particle yields were set by changing the separator parameters or polyethylene plates. After the new energy were set, the process was repeated from the start.

4.1 Energy and efficiency calibrations

The cross sections depend only on the relative ratio of discrete events, between the dE-detector and the spectrometer, so calibrations for this experiment, were not as important as they are usually. The main goal with the calibrations was to determine the spectrometer's absolute efficiency. The calibrations were also used to set up correct biases and amplifier settings to match the CsI(Tl)-detectors as well as to fix the energy channel of the dE-detector. Precise settings can be found on appendix A.

^{60}Co source was used for all the calibrations. It was placed in the middle of the spectrometer array, in the position of the actual target. A $CeBr_3$ detector, with dimensions 51 mm $\times$ 51 mm $\times$ 51 mm was placed 10 cm behind the source. Time signal from the $CeBr_3$ detector was used to start the data acquisition.

Cobalt-60 beta decays to 4^+ state of nickel-60 with 98.8% probability. The excited state of nickel-60 then decays by emitting two gammas in series, first one at 1.17 MeV and another one at 1.33 MeV. It was assumed that both gammas were emitted isotropically to different directions in space. If the $CeBr_3$ detector saw an event at 1.33 MeV, a corresponding gamma at 1.17 MeV must have been emitted slightly earlier. Traces of this gamma, could be then looked for in the spectrometer.

The data analysis was done using ROOT, in a similar manner as the actual

measurements. Due to how the data acquisition was set-up, events in the $CeBr_3$ detector and in the spectrometer were time correlated on the output data files. Gating condition was set to the 1.33 MeV peak on the $CeBr_3$ detector's energy channel and what events were left on the spectrometer's channels were counted.

The efficiency was calculated by dividing the number of events in the spectrometer with the the total counts inside the $CeBr_3$'s gate. This process was also done to different multiplicities to get independent efficiencies for them. As expected, the total efficiency of our CsI(Tl) spectrometer was around 85%, which was slightly lower than the geometric efficiency of 92%. It should be noted that some additional corrections maybe required due to neutron emission anisotropy and breakup of the heavy nuclei without emission of gamma quanta.

The energy channel of the dE-detector had to be calibrated, since it was needed for calculating the collision energies at the target. The detector was calibrated to the doublet of ^{60}Co using linear extrapolation. The absolute efficiency of the dE-detector did not matter in this case, because the data acquisition was actually triggered by it. Thus, even if some particles slip past the dE-detector and reacted with the target, they were not being recorded. The low intensity also helped with this. The distance between incoming particles should have been long enough, that the spectrometer would not get too many false readings.

4.2 Analyzing the data with ROOT

After a successfully triggered event, the USB-interface box / crate controller (CC-USB) read the stored data from the buffer memories of the ADC and TDC modules. Thirty channels in total, per each event. The interface then converted the collected data into USB serial format and send them over to the computer in set packets. These packets contained the individual readings in 16-bit hex-words, followed by a end of packet marker word (43605 or hex 0xAA55). On the PC, a control software for the CC-USB module (XXUSBWin) stored the data in 20 MB binary files.

The data in the channels was as follows. Channel 1: the energy loss in dE-detector. Channels 2-3: not used in the analysis. Channel 4: the time of flight between the TOF stop and the active collimator detector. Channel 5: the high resolution time of flight between. Channel 6: not used. ACCULINNA's TOF-detectors. Channels 7 – 18: energy signals from the spectrometer's CsI(Tl)-detectors. Channels 19 – 30: time signals from the spectrometer's CsI(Tl)-detectors.

The analysis began by converting the binary data to .root format for easier handling with ROOT's built-in functions. 14 plots were drawn: ch1–ch4 (dE–collimation), ch1–ch5 (dE–TOF) and ch7;18–ch19;30 (E–T) plots for all 12 CsI(Tl)-detectors. Entries were time correlated and gating conditions was be set for extracting the total number events of each isotope and their corresponding reaction gammas (Fig. 9).

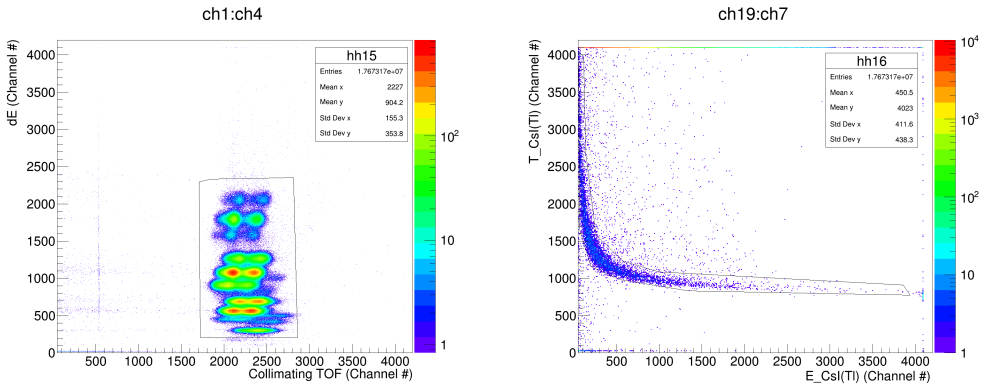

(a) Setting the collimating condition. **(b)** Gating on one of E–T plots.

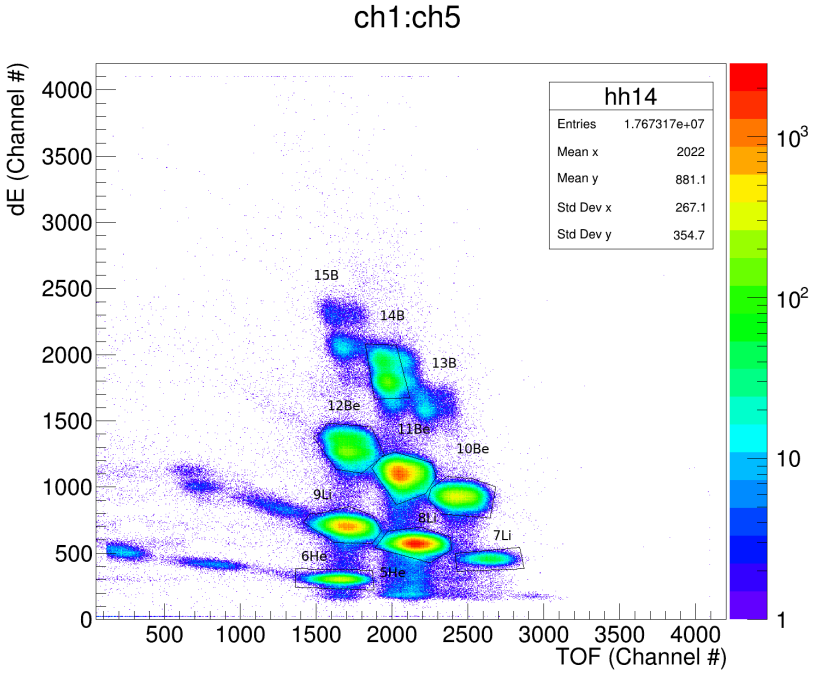

(c) Gating of different isotope peaks on the dE–TOF plot.

Figure 9. The gating conditions (black lines) could be set graphically with ROOT. Some additional isotopes could be seen, but most of them were cut out by the collimation condition, since they were not flying towards the target

Same set of gating contours were used for all measurements at the same energy to get consistent data. The collimation conditions were set up so that all the events caused by the beam were selected (Fig. 9a). On the dE-TOF plot, all the isotopes, clearly visible and recognizable, were gated with their own contours (Fig. 9c). On the E–T plots, the main curves were traced (Fig. 9b).

To verify and estimate the reliability of the results, the data analysis was done with many contours and by different people. The results varied only within the error margins. The analysis also revealed that it did not matter how precisely the isotopes on dE–TOF graph were gated or if there were any threshold set for the backscattering on the E–T graphs. This was really good, as it gave more credibility to the analysis method.

4.3 Calculating the collision energy using LISE++

It was not possible to directly measure the collision energy at the target plane. However, assuming the average energy loss in the dE-detector, it could be calculated theoretically. This was done using LISE++ program's physical calculator (Fig. 10).

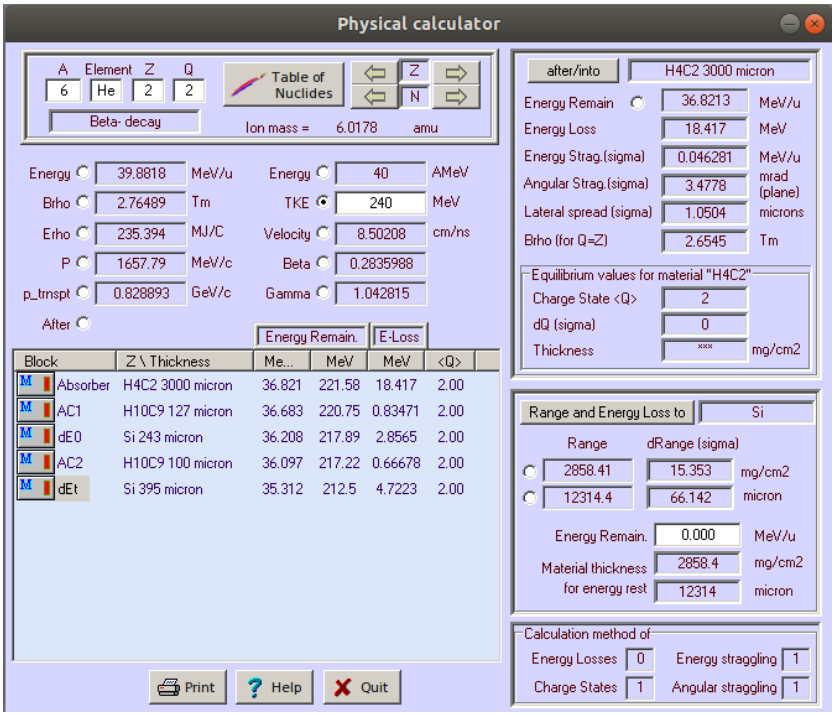

Figure 10. The collision energies were calculated with LISE++'s physical calculator. In this figure they are being calculated for ^{6}He on silicon target.

The physical construction of the setup was set to the calculator. Some value for the total kinetic energy of the projectile at the start was guessed and the program calculated the energies and energy losses at different points of the setup. These results were then compared to the measured data. The total energy was altered by hand, until the energy loss in the simulated dE-detector matched the measured value.

The average collision energy for that specific isotope in that particular run could then be read from the target column of LISE++'s calculator. Thickness of the target was halved, as it was assumed that the reactions would be taking place, on average, at the center of the target.

The error of the collision energy was approximated to be the energy loss in half of the target's thickness. In reality it may have been slightly larger due to other errors sources, such as energy spread of the beam, which was usually around 100 keV u^{-1}. In any case, the error of the collision energies tended to be quite small with this setup (<1 MeV u^{-1}) and not terribly important for the accuracy of the final results.

4.4 Cross section calculations

The ROOT script printed out a text file, containing the number of total triggered events, corresponding entries in the spectrometer, sorted by the multiplicity (how many CsI(Tl)-detectors were triggered) and the average energy loss in the dE-detector. The data was gathered into spreadsheets for easier handling. (Fig. 11).

Run #	Target	Beam	Total	m1	m2	m3	m4	m5	m6	m7	m8	m9	m10	m11	m12	Sigma (mb)	sigma error	energy (MeV/A)	energy error (MeV/A)	error (MeV)
5	Si	1533467	10774	4472	2237	1606	1061	673	424	181	77	28	12	3	0	1612.487856369	18.85436561	34.945	0.793233333333333	4.7594
6	background	532318	1201	888	151	93	31	21	11	4	1	1	0	0	0	0				
7	Si	519797	3574	1481	779	555	326	216	99	73	29	13	3	0	0	1576.887165964	12.02464617	28.886	0.917083333333333	5.5025
8	background	221134	489	376	53	22	20	14	1	2	0	1	0	0	0	0				
9	Si	9317	77	33	13	12	7	8	3	1	0	0	0	0	0	2099.457316815	82	276.0046457	25.905	0.995066666666667	5.9704
10	background	217296	437	341	49	19	7	12	6	2	1	0	0	0	0	0				
11	Co	521206	1713	926	205	137	120	124	78	60	40	15	7	1	0	2453.150789700	5	96.79528781	26.6444	0.254266666666667	1.5256
12	background	144390	306	234	34	17	12	5	3	1	0	0	0	0	0	0				
13	Ta	188270	761	311	87	42	46	38	33	36	43	46	44	26	9	3846.360636756	5	198.8260053	26.3222	0.577133333333333	3.4629
14	Ta	285297	1156	479	118	70	56	48	60	91	65	72	55	30	12	4068.968593363	98	166.1239748	22.002	0.654566666666667	3.9274
15	background	224722	438	351	42	18	12	7	3	1	2	1	1	0	0	0				
16	Si	313819	2307	904	500	355	264	151	79	33	15	5	0	1	0	1826.33417002977	44	35590253	21.512	1.14625	6.8775
17	Co	142258	455	244	53	35	42	29	17	12	15	4	3	0	1	2486.989732270	95	186.5500817	22.365	0.2909	1.7454
18	Co	65558	210	112	32	13	12	6	18	8	6	1	1	1	0	1907.476044950	6	240.6653101	31.236	0.226116666666667	1.3567
19	Si	76091	555	240	110	81	46	38	23	11	3	2	1	0	0	1706.845267063	77	87.08259163	30.588	0.876916666666667	5.2615
20	background	153226	344	270	38	14	12	4	3	2	0	1	0	0	0	0				
21	Ta	118527	526	215	47	37	37	26	25	31	37	23	25	15	8	4242.952058204	29	263.1868364	30.947	0.51625	3.0975
22	Si	112185	845	352	183	121	87	49	34	9	9	1	0	0	0	1676.109230908	02	71.06973204	24.728	1.03225	6.1935
23	Ta	94859	432	204	47	22	20	17	11	23	24	30	17	13	4	3830.993683585	07	279.5472308	25.162	0.596816666666667	3.5809
24	background	201999	520	396	75	27	7	8	4	2	1	0	0	0	0	0				
25	Ta	61308	294	125	26	18	18	10	25	14	16	15	18	7	2	4297.965991249	95	368.308431	25.162	0.596816666666667	3.5809
26	Co	209703	730	387	91	70	46	53	33	19	21	5	4	1	0	1805.202739135	55	130.9053713	25.494	0.2637	1.5822
27	Ta	157690	663	269	76	50	35	35	27	34	33	43	28	24	9	3370.486356448	59	203.3681592	27.565	0.559866666666667	3.3592
28	Si	240557	1797	718	374	268	184	131	63	39	15	3	2	0	0	1692.893364861	21	48.77606009	27.164	0.961516666666667	5.7691
29	background	178268	439	318	50	37	14	11	1	2	5	1	0	0	0	0				
30	Co	359405	1397	767	182	129	105	80	50	46	17	14	6	1	0	2835.464210319	93	125.3189722	27.877	0.246283333333333	1.4777
31	Ta	70748	484	198	66	20	13	8	8	10	14	7	23	16	8	6255.442550479	09	475.1730965	26.513	0.5742	3.4452
32	Si	178537	1328	571	257	200	134	78	41	28	15	2	1	0	1	1644.173093982	57	55.79696377	26.1	0.989183333333333	5.9351
33	background	353818	911	684	104	62	29	19	8	1	3	1	0	0	0	0				
34	background (Run 24)	548162	1398	1071	189	65	32	17	16	1	5	2	0	0	0	0				
35	Ta (Run 25)	229131	1032	457	107	66	43	53	49	49	60	40	57	38	13	3780.249132667	65	178.67222	25.162	0.596816666666667	3.5809
36	Ta (Run 21)	680934	3078	1337	358	213	166	135	140	139	143	168	151	100	28	4402.500154554	38	111.8499843	30.947	0.51625	3.0975
37	Co (Run 26)	1172940	4232	2357	522	363	282	239	182	120	94	45	22	5	1	2105.477721709	7	59.77701485	25.494	0.2637	1.5822
24+34	background	750161	1918	1467	264	92	39	25	20	3	6	2	0	0	0	0				
23+25+35	Ta	385298	1758	786	180	106	81	80	85	86	100	85	92	58	19	3881.419580789	6	139.6161527	25.162	0.596816666666667	3.5809
26+37	Co	1382643	4962	2744	613	433	328	292	215	139	115	50	26	6	1	2094.333443320	5	54.38476236	25.494	0.2637	1.5822
22	Si	112185	845	352	183	121	87	49	34	9	9	1	0	0	0	1682.020553667	32	71.19494654	24.728	1.03225	6.1935

Figure 11. Example of the excel sheets filled with data. Calculations were grouped by the energy (same color) and by projectile (in different spreadsheets).

The total cross sections were calculated using a following formula:

$$\sigma_R = \frac{I_\gamma - \frac{I}{I_b} I_{b\gamma}}{\eta n I} c, \tag{1}$$

where I_γ is the number of measured gammas, $I_{b\gamma}$ is the measured gammas without the target (background), I_b is the total number of events on background run i.e. total counts on the dE-detector. I indicates the total events with the target, η is the efficiency of the spectrometer, n is the number of target nuclei per unit area (number density times thickness, calculated using LISE++) and c is the conversion coefficient to millibarns.

This is a common linear approximation for calculating the cross section with a stationary thin target, where on average, the incoming particle interacts only once with the target nucleus. The purpose of the term $\frac{I}{I_b} I_{b\gamma}$ is to negate noise by normalizing the events to the background run.

Calculating the cross sections this straightforwardly, may have been an oversimplification. To assess how reliable the results given by this approach were, more sophisticated method was also used. The yields for different multiplicities were used to calculate the partial cross sections, which were then added together to get the total cross section. The efficiency of the array increases depending on how many detectors were triggered, each of the twelve multiplicities had different efficiency coefficient, which were determined during the calibration with the ^{60}Co source.

These cross sections fell within the error margins of the earlier results, which confirmed the feasibility of the first approach. Some even more sophisticated theoretical calculations were also used, but they are not dealt with in this thesis.

Errors of the cross sections for the preliminary results were quickly determined by a simple statistical approach using an estimate for standard error of the mean, which gave a good first order approximation

$$\delta\sigma_R = \frac{\sigma_R}{\sqrt{I_\gamma - \frac{I}{I_b} I_{b\gamma}}}. \tag{2}$$

In reality, there are additional error sources, such as uncertainty of the efficiency and errors from the electronics. More comprehensive error analysis will be done for the final results.

5 Preliminary results and discussion

In this section, a brief look at the preliminary results is taken. The results are considered only from the practical point of view, to evaluate the capability of setup and methods used. Theoretical interpretation and possible implications of the results are outside the scope of this work and left for future publications.

At the time of writing, the verification and theoretical analysis of the final results is still ongoing. The preliminary results, however, seem to be promising. All the plots and values shown in this work are calculated by the author, using tools and method described in the previous sections. The contours and thresholds (in this case no threshold at all), used in these calculations were also set by the author and thus the values presented here may slightly differ from the final results.

5.1 Quick inspection of the results

In figure 12, preliminary results for cross sections of ^{6}He on silicon (blue triangle) are plotted along with the results from multiple previous measurements. New values seem to fit well with the past results, confirming the correct operation of the setup. Numerical results for all measured isotopes can be found on the appendix C.

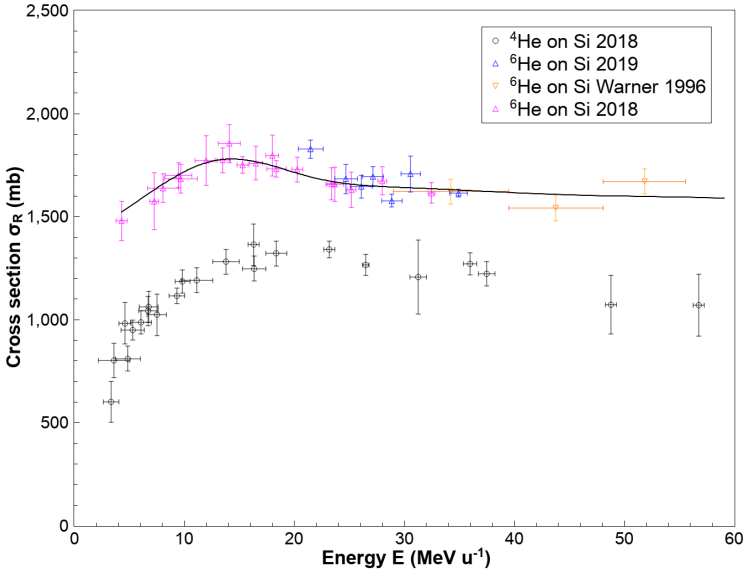

Figure 12. Cross section of different helium isotopes. The enhancement of the total reaction cross section for ^{6}He is clear. The bump is thought to be caused by the weakly bound nucleons and the resulting shell structure [3], [5], [31].

5.2 Problems and possible future improvements

The biggest problem of this setup was distinguishing between the real reaction events and the background counts. Even though extra attention was given to the shielding of the spectrometer along with the active collimator system, some noise was still seen in the data. The interactions between the projectiles and target nuclei were relatively rare, which meant that even a low background distorted the results.

In each run, depending on the projectile, target and energy, between 25 and 60 percent of the events counted by the spectrometer were attributed to noise. Majority of the noise had multiplicity of one and it dramatically dropped towards the higher orders. The same effect was seen even during the background and calibration runs, when no target was present.

Most of the first order multiplicity noise was less than 150 keV and it extended across the whole time domain (Fig. 13, left). This suggested that it may have been of electric origin, i.e. from the cables or electronics. Moreover, this noise was not evenly spread across the detectors, but it varied a lot. The third CsI(Tl)-detector was especially noisy. It alone was a huge contributor to the overall noise as on some runs, it counted five times more than other detectors.

For the higher multiplicities, nature of the noise changed. It now laid on the same E–T curve as the real events, which implied a different source (Fig. 13, right). Counts in the detectors also leveled out for higher multiplicities, indicating that this time they were caused by actual hits from particles, rather than the electronics. Most likely, the culprit behind this higher order noise was the AC-detector, as the collimation system cannot get rid of stray particles if it itself is causing them.

In fact, this may be inherit problem with this setup and cannot be solved without rethinking everything. If the AC-detector is too far away from the target, the beam will disperse before it reaches it. On the other hand, if the detector is too close, it will be inside the sensitive zone of the spectrometer. Make it too small and the yield drops impractically low. Luckily the contribution of this noise to overall background was rather small, less than 5%.

The best way to improve the results, without changing the whole setup, would be to track down the source of the low energy noise and collect more statistics. However, collecting more statistics, means either longer measurements or increasing the beam intensity and yield. Both options are not really viable as the measurements were already quite lengthy and only limited amount of beam time was available.

Increasing the intensity and yield on the other hand is not a trivial task and it would probably cause more problems than it could solve anyway.

Linear normalization to background is valid, only if the noise behaved accordingly. To proof that this was the case, the calculations were repeated with various different thresholds and contours, and even with no thresholds at all. Fortunately the noise behaved very linearly and with enough statistics our normalization worked very well. The results did not change significantly depending on the chosen contours and threshold, but they staid within the error margins. Had the noise not been linear, the results would have been skewed.

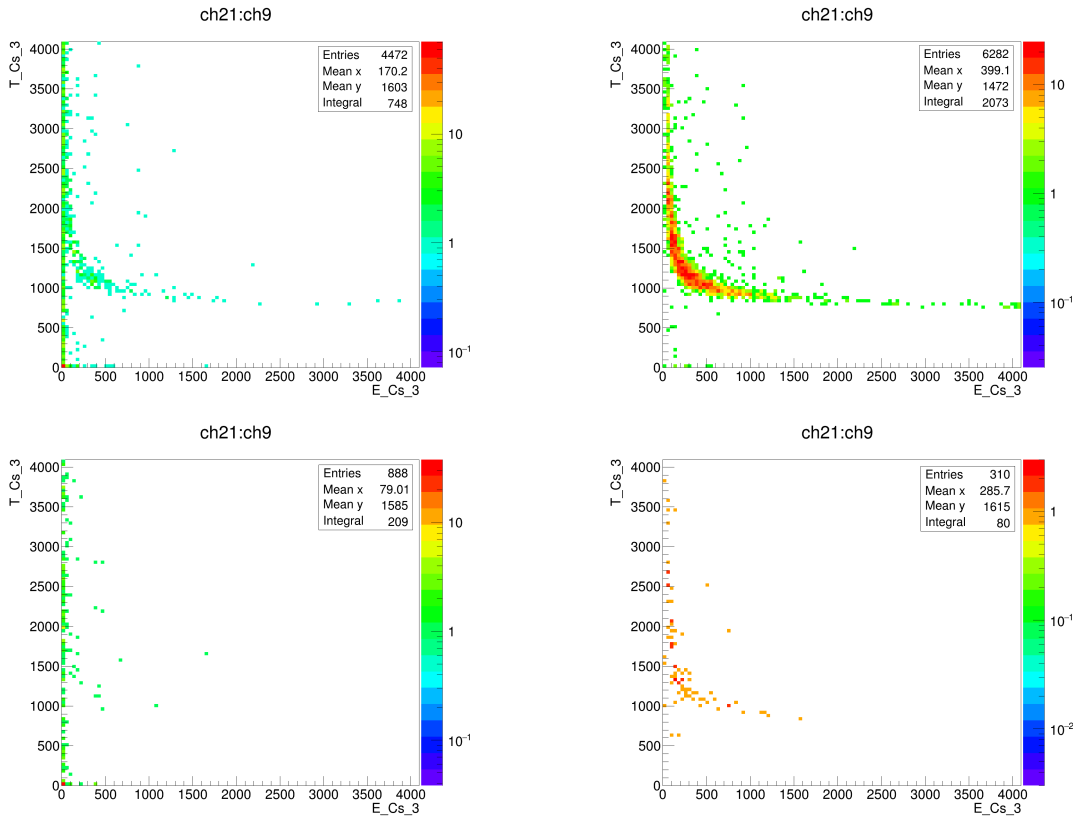

Figure 13. Distribution of the noise on third CsI(Tl)-detector for the ^{6}He on silicon target (top) and corresponding background runs (below). On left, all counts for multiplicity one. On the right, all higher multiplicities from 2–12. The behavior of the noise changed significantly towards higher multiplicities. The low energy noise was present on the whole time domain, in all measurements, even without the target. The third detector was a lot noisier than the others, which may have been due to bad electronics.

Another, slightly trickier problem would be assessing the determined efficiency of the spectrometer. The cobalt source, which was used for the calibrations, may have not produced same kind of signature distribution as the exotic neutron heavy nuclei. The cross sections may be slightly underestimated, if majority of the neutrons fly in small forward angles instead of spreading isotropically.

The rear detectors (after the target) had little more counts, which may have been an indication of slight anisotropy of the reactions. Breakup of the neutron heavy nuclei, without emission of gamma quanta, could also be possible. However, this should not refute the evidence for the observed enhancements of the cross sections, in fact they may be even stronger, if some of the reactions go undetected.

Perhaps more accurate efficiency could be calculated using theoretical models or with GEANT4 simulations [32]. However, any systematic error in the results should be revealed when comparing to preexisting cross sections and appropriate corrections could be made. Thus far, no indication of systematic error has been seen.

Doubling up the detectors in the gamma spectrometer, from previous 6 to 12, appears to have improved the overall efficiency by 15% from 70% to 85% [5]. Majority of this improved gain, would be at the problematic low angles and since the increase in efficiency was just as the test GEANT4 calculations predicted, it is save to say that the cross sections should not be too far off and the assumptions made about the isotropicity are reasonably valid.

Less critical perturbations was also observed during the measurements. These include some odd artifacts in the data plots. For example, sometimes "shadows" were seen in the dE–TOF graphs (Fig. 14).

Shadows, in this context, meaning that additional peaks were seem behind the primary groups. These were probably due to drifting of the separator or cyclotron magnets and dispersion or reflections from the setup itself. Similar drift was seen in the time channel of the gamma detectors during the calibration run (Fig. 15). This was probably due to bad connection or movement of the ^{60}Co source.

These shadows, were ended up not being a huge problem as the disappeared almost completely once the collimation condition was set. This meant that, even if some of them were accidentally included in the isotope gating, they did not persist and alter the results.

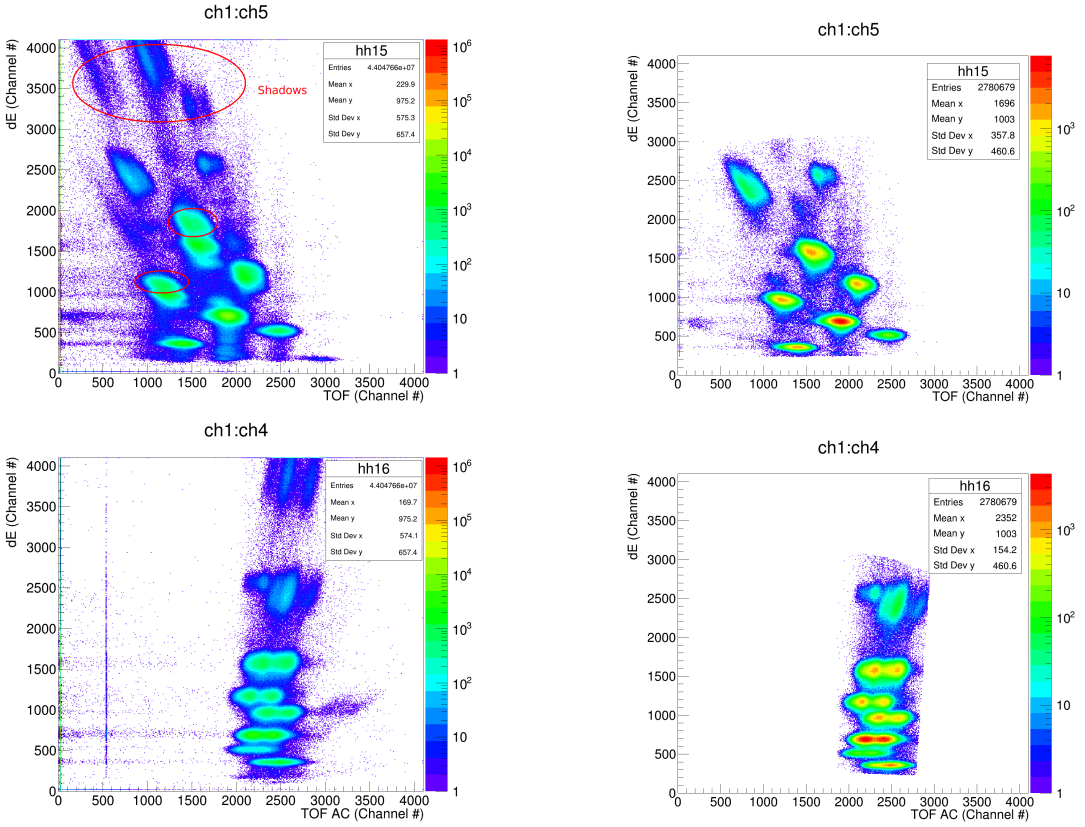

Figure 14. Cleanup of the shadows in the data. On the left side unfiltered data, in which a lot of noise is present. On the right side, same data after gating the channels applying the collimation condition.

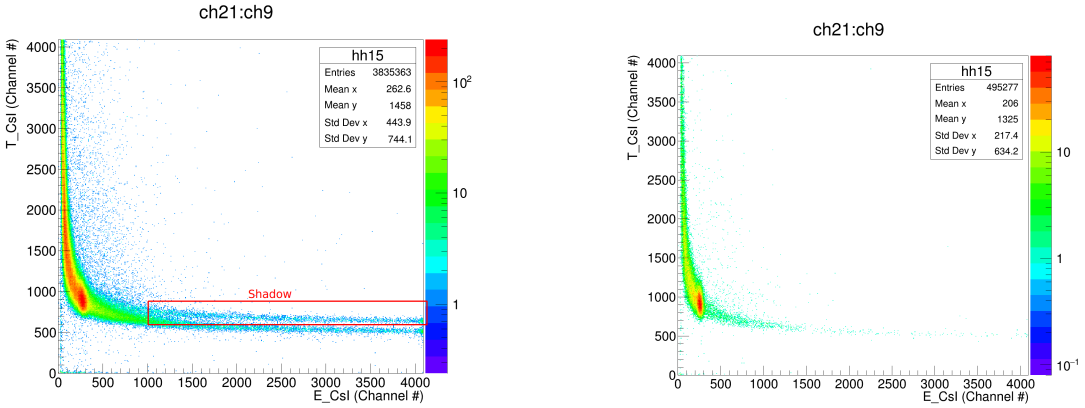

Figure 15. Time shifted shadow tail, as seen in one of the E–T plots during ^{60}Co calibration run. It was probably caused by shifted source or a cable. On the right, same plot after gating to the 1337 keV peak.

6 Conclusions

Total reaction cross sections for ^{6}He, $^{7-9}$Li, $^{10-12}$Be and ^{14}B isotopes on ^{28}Si, ^{181}Ta, ^{59}Co targets were measured for energies between 10 – 60 MeV u^{-1}. In total, 120 different cross sections were successfully extracted. Cross checking the results with some of the known values confirmed the correct operation of the new setup and validity of the analyzing methods. Moderate statistical errors were present in some of the results, due to background, but they can still be very useful for testing a wide range of different theoretical microscopic nuclear models.

For some reactions, such as ^{6}He + ^{181}Ta and ^{6}He + ^{59}Co, earlier data could not be found. This was likely the first time those were experimentally measured. They may be useful for improving the cascade excitation models used in particle simulations, such as GEANT4. These simulations have far-reaching uses, all the way from research to medical applications. For example, they can used for modeling the radiation rigidness of the next generation semiconductors.

Overall, the experiment was a success, but far from perfect. The setup still needs further refinements to bring down the error bars for more accurate results. The absolute efficiency of the spectrometer was also difficult to estimate accurately.

In any case, no experiment is perfect and despite the problems. While the new cross section data seems to be valid, this experiment also gave valuable experience and new measurements with improved setup is already being planned.

References

[1] Y. G. Sobolev, M. P. Ivanov, and Y. E. Penionzhkevich, "A setup for measuring total cross sections of nuclear reactions", *Instruments and Experimental Techniques Vol. 55 No. 6*, 2012. DOI: 10.1134/S0020441212050168.

[2] Y. G. Sobolev *et al.*, "Studying the excitation function of the full cross section of a reaction using a modified transmission technique: Initial results", *Bulletin of the Russian Academy of Sciences. Physics Vol. 76 No. 8*, 2012. DOI: 10.3103/S1062873812080254.

[3] Y. E. Penionzhkevich *et al.*, "Peculiarities in total cross sections of reactions with weakly bound nuclei ^{6}He, ^{9}Li", *Physics of Atomic Nuclei Vol. 80 No. 5*, 2017. DOI: 10.1134/S1063778817050210.

[4] Y. G. Sobolev *et al.*, "Experimental study of the energy dependence of the total cross section for the ^{6}He + ^{nat}Si and ^{9}Li + ^{nat}Si reactions", *Physics of Particles and Nuclei Vol. 48 No. 6*, 2017. DOI: 10.1134/S1063779617060545.

[5] Y. E. Penionzhkevich *et al.*, "Energy dependence of the total cross section for the ^{11}Li + ^{28}Si reaction", *Physical Review C 99 014609*, 2019. DOI: 10.1103/PhysRevC.99.014609.

[6] A. I. Baz, *Adv. Phys. 8. 349*, 1959.

[7] I. Tanihata *et al.*, "Measurements of interaction cross sections and nuclear radii in the light p-shell region", *Physical Review Letters Vol. 55 No. 24*, 1985.

[8] P. G. Hansen and B. Jonson, "The neutron halo of extremely neutron-rich nuclei", *Europhys. Lett. 4 (4)*, 1987. DOI: 10.1209/0295-5075/4/4/005.

[9] A. S. Demyanova *et al.*, "Use of (^{3}He;t) charge-exchange reactions in determining radii of excited states of nuclei", *Physics of Atomic Nuclei Vol. 80 No. 5*, 2017. DOI: 10.1134/S1063778817050064.

[10] Z. T. Lu *et al.*, "Laser probing of neutron-rich nuclei in light atoms", *Reviews of Modern Physics Vol 85*, 2013. DOI: 10.1103/RevModPhys.85.1383.

[11] T. L. Belyaeva *et al.*, "Determination of neutron halo radii in the first excited states of ^{13}C and ^{11}Be with the asymptoticnormalization coefficients method", *Physical Review C 90 064610*, 2014. DOI: 10.1103/PhysRevC.90.064610.

[12] A. A. Ogloblin *et al.*, "Effect of neutron halos on excited states of nuclei", *Physical Review C 84 054601*, 2011. DOI: 10.1103/PhysRevC.84.054601.

[13] Z. H. Liu *et al.*, "Asymptotic normalization coefficients and neutron halo of the excited states in ^{12}B and ^{13}C", *Physical Review C Vol. 64*, 2001. DOI: 10.1103/PhysRevC.64.034312.

[14] Z. H. Liu, X. Z. Zhang, and H. Q. Zhang, "Nuclear halo and its scaling laws", *Physical Review C 68 024305*, 2003. DOI: 10.1103/PhysRevC.68.024305.

[15] J. G. Chen *et al.*, "Halo or skin in the excited states of some light mirror nuclei", *Eur. Phys. J. A 23*, 2005. DOI: 10.1140/epja/i2004-10074-0.

[16] R. Sánchez *et al.*, "Nuclear charge radii of $^{9;11}$Li: The influence of halo neutrons", *PRL 96 033002*, 2006. DOI: 10.1103/PhysRevLett.96.033002.

[17] W. Nörtershäuser *et al.*, "Nuclear charge radii of $^{7;9;10}$Be and the one-neutron halo nucleus ^{11}Be", *Physical Review Letters 102 062503*, 2009. DOI: 10.1103/PhysRevLett.102.062503.

[18] A. A. Ogloblin *et al.*, "Observation of abnormally large radii of nuclei in excited states in the vicinity of neutron thresholds", *Physics of Atomic Nuclei Vol. 74 No. 11*, 2011. DOI: 10.1134/S1063778811110147.

[19] S. A. Goncharov *et al.*, "Analogues of the exotic hoyle state in the ^{12}C nucleus", *Moscow University Physics Bulletin Vol. 70 No. 5*, 2015. DOI: 10.3103/S0027134915050057.

[20] A. A. Ogloblin *et al.*, "Nuclear states with anomalously large radius (size isomers)", *Physics of Atomic Nuclei Vol. 79 No. 4*, 2016. DOI: 10.1134/S1063778816040177.

[21] T. L. Belyaeva *et al.*, "Neutron halos in the excited states of ^{12}B", *Physical Review C 98 034602*, 2018. DOI: 10.1103/PhysRevC.98.034602.

[22] K. Riisager, "Halos and related structures", *Phys. Scr.*, 2012. eprint: arXiv:1208.6415v1.

[23] A. S. Jensen and K. Riisager, "Towards necessary and sufficient conditions for halo occurrence", *Physics Letters B 480*, 2000. DOI: 10.1016/S0370-2693(00)00413-5.

[24] A. A. Ogloblin *et al.*, "Nuclear states with abnormal radii", *The 3rd International Conference on Particle Physics and Astrophysics KnE Energy and Physics*, 2018. DOI: 10.18502/ken.v3i1.1716.

[25] L. M. Kerby and S. G. Mashnik, "Total reaction cross sections in CEM and MCNP6 at intermediate energies", *Nuclear Instruments and Methods in Physics Research B*, 2015. eprint: arXiv:1505.00842v1.

[26] S. Leray *et al.*, "Results from the IAEA benchmark of spallation models", *Journal of the Korean Physical Society Vol. 59 No. 2*, 2011. DOI: 10.3938/jkps.59.791.

[27] *ACCULINA*. [Online]. Available: http://aculina.jinr.ru/.

[28] A. M. Rodin *et al.*, "Status of ACCULINNA beam line", *Nuclear Instruments and Methods in Physics Research B 204*, 2003. DOI: 10.1016/S0168-583X(02)01897-9.

[29] *LISE++*. [Online]. Available: http://lise.nscl.msu.edu/lise.html.

[30] *Cern ROOT*. [Online]. Available: https://root.cern.ch/.

[31] R. E. Warner *et al.*, "Total reaction and 2n-removal cross sections of 20-60 AMeV $^{4;6;8}$He $^{6-9,11}$Li and ^{10}Be on si", *Physical Review C Vol. 54 No. 4*, 1996. DOI: 10.1103/physrevc.54.1700.

[32] *GEANT4*. [Online]. Available: https://geant4.web.cern.ch/.

A Settings of the gamma detectors

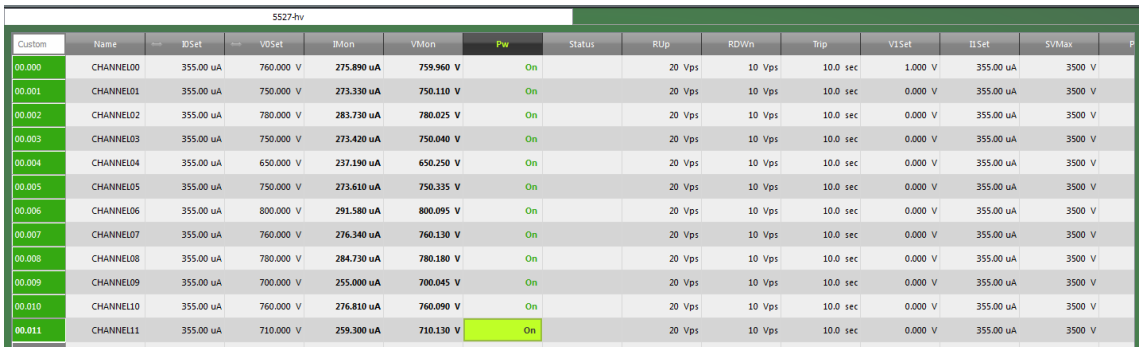

5527-hv

Custom	Name	IOSet	VOSet	IMon	VMon	Pw	Status	RUp	RDWn	Trip	V1Set	I1Set	SVMax
00.000	CHANNEL00	355.00 uA	760.000 V	275.890 uA	759.960 V	On		20 Vps	10 Vps	10.0 sec	1.000 V	355.00 uA	3500 V
00.001	CHANNEL01	355.00 uA	750.000 V	273.330 uA	750.110 V	On		20 Vps	10 Vps	10.0 sec	0.000 V	355.00 uA	3500 V
00.002	CHANNEL02	355.00 uA	780.000 V	283.730 uA	780.025 V	On		20 Vps	10 Vps	10.0 sec	0.000 V	355.00 uA	3500 V
00.003	CHANNEL03	355.00 uA	750.000 V	273.420 uA	750.040 V	On		20 Vps	10 Vps	10.0 sec	0.000 V	355.00 uA	3500 V
00.004	CHANNEL04	355.00 uA	650.000 V	237.190 uA	650.250 V	On		20 Vps	10 Vps	10.0 sec	0.000 V	355.00 uA	3500 V
00.005	CHANNEL05	355.00 uA	750.000 V	273.610 uA	750.335 V	On		20 Vps	10 Vps	10.0 sec	0.000 V	355.00 uA	3500 V
00.006	CHANNEL06	355.00 uA	800.000 V	291.580 uA	800.095 V	On		20 Vps	10 Vps	10.0 sec	0.000 V	355.00 uA	3500 V
00.007	CHANNEL07	355.00 uA	760.000 V	276.340 uA	760.130 V	On		20 Vps	10 Vps	10.0 sec	0.000 V	355.00 uA	3500 V
00.008	CHANNEL08	355.00 uA	780.000 V	284.730 uA	780.180 V	On		20 Vps	10 Vps	10.0 sec	0.000 V	355.00 uA	3500 V
00.009	CHANNEL09	355.00 uA	700.000 V	255.000 uA	700.045 V	On		20 Vps	10 Vps	10.0 sec	0.000 V	355.00 uA	3500 V
00.010	CHANNEL10	355.00 uA	760.000 V	276.810 uA	760.090 V	On		20 Vps	10 Vps	10.0 sec	0.000 V	355.00 uA	3500 V
00.011	CHANNEL11	355.00 uA	710.000 V	259.300 uA	710.130 V	On		20 Vps	10 Vps	10.0 sec	0.000 V	355.00 uA	3500 V

Figure 16. Bias voltages and offsets for the CsI(Tl)-detector's PMTs.

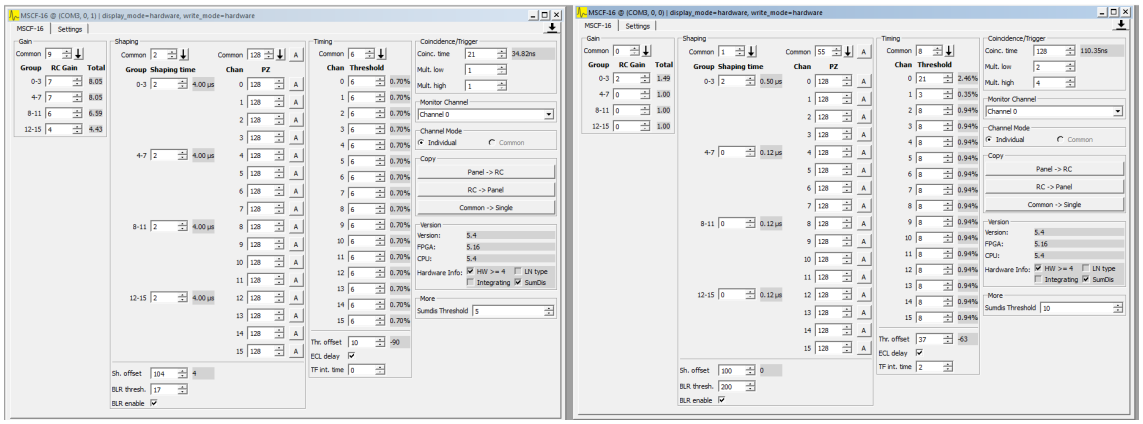

Figure 17. Gain, shaping time, thresholds, coincidence etc. settings for the CsI(Tl) amplifiers.

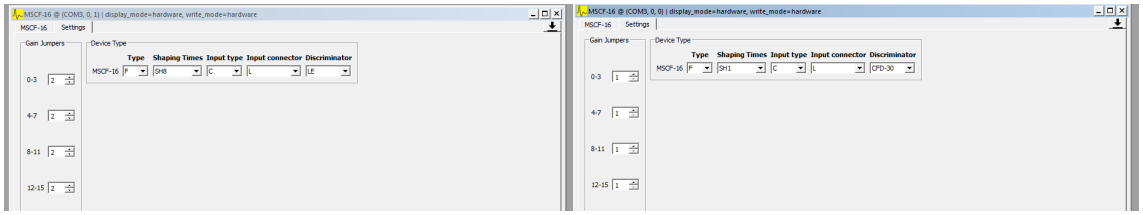

Figure 18. Gain, shaping time, thresholds, coincidence etc. settings for the CsI(Tl) amplifiers continued. All the settings were about the same as in the previous experiment, done late 2018 [5].

B List of equipment

Preamplifier (PA)	Mesytec MPR-1
High-voltage supply (HV)	Polon 1904
Programmable high-voltage supply (PHV)	CAEN SY5527 + AG7435N
Spectroscopy amplifier (DSA)	Ortec 855
Timing filter amplifier (TFA)	Ortec 863
Time-to-amplitude converter (TAC)	Ortec 566 and Polon 1701
Constant fraction discriminator (CFD)	GSI CF4000
Delay line (DL)	Coaxial cable
Programmable TFA+CFD (MSCF)	Mesytec MSCF-16
Time-to-digital converter (TDC)	Phillips 7186H
Peak analog-to-digital converter (PADC)	Phillips 7164
Master trigger (MT)	KL-24K
Logic level translator (LT)	GSI LA8010
Gate generator (GG)	GSI GG8020
Fan-in / fan-out (LP)	LeCroy 428F
CAMAC crate controller (CC-USB)	WIENER CC-USB
Backplane (BP)	WIENER CAMAC crate

C Preliminary results in tables

Table 1. ^{6}He cross sections on silicon.

Energy MeV u^{-1}	*Error* MeV u^{-1}	*Cross Section* mb	*Error* mb
21.5	1.1	1826	44
24.7	1	1682	71
26.1	1	1644	56
27.2	1	1693	49
28.9	0.9	1577	32
30.6	0.9	1707	87
34.9	0.8	1612	19

Table 2. ^{6}He cross sections on tantalum.

Energy MeV u^{-1}	*Error* MeV u^{-1}	*Cross Section* mb	*Error* mb
22	0.7	4069	166
25.2	0.6	3881	140
26.3	0.6	3846	199
27.6	0.6	3370	203
30.9	0.5	4403	112

Table 3. ^{6}He cross sections on cobalt.

Energy MeV u^{-1}	*Error* MeV u^{-1}	*Cross Section* mb	*Error* mb
22.4	0.3	2487	187
25.5	0.3	2105	60
26.6	0.3	2453	97
27.9	0.2	2835	125
31.2	0.2	1907	241

Table 4. ^{7}Li cross sections on silicon.

Energy MeV u^{-1}	*Error* MeV u^{-1}	*Cross Section* mb	*Error* mb
44.3	1.3	2140	475
46.7	1.2	1620	140
48.3	1.2	1602	112
49.9	1.2	1489	327
50.2	1.2	1468	92
54	1.1	1645	292
55.1	1.1	1083	184
62.4	1	1388	160

Table 5. ^{7}Li cross sections on tantalum.

Energy MeV u^{-1}	*Error* MeV u^{-1}	*Cross Section* mb	*Error* mb
47.1	0.7	3808	337
48.8	0.7	4985	509
50.7	0.7	3387	414
55.5	0.7	4584	360

Table 6. ^{7}Li cross sections on cobalt.

Energy MeV u^{-1}	*Error* MeV u^{-1}	*Cross Section* mb	*Error* mb
47.6	0.2	1857	137
51.1	0.3	2233	226
55.9	0.3	1591	584

Table 7. ^{8}Li cross sections on silicon.

Energy MeV u^{-1}	*Error* MeV u^{-1}	*Cross Section* mb	*Error* mb
24.9	1.7	1805	59
31.9	1.4	1664	30
32.5	1.4	1762	40
34.1	1.4	1609	34
36.1	1.3	1657	21
37.9	1.3	1656	32
41.7	1.2	1653	33
47.9	1	1609	18

Table 8. ^{8}Li cross sections on tantalum.

Energy MeV u^{-1}	*Error* MeV u^{-1}	*Cross Section* mb	*Error* mb
25.7	1	3663	211
32.5	0.8	3738	75
33.1	0.8	3749	231
34.7	0.8	3405	85
36.7	0.8	3833	94
42.2	0.7	3889	96
42.6	0.3	4126	71

Table 9. ^{8}Li cross sections on cobalt.

Energy MeV u^{-1}	*Error* MeV u^{-1}	*Cross Section* mb	*Error* mb
26.2	0.4	2954	265
33	0.4	2229	37
33.5	0.4	2002	103
37.1	0.3	2485	51
42.6	0.3	2378	102

Table 10. ^{9}Li cross sections on silicon.

Energy MeV u^{-1}	*Error* MeV u^{-1}	*Cross Section* mb	*Error* mb
18	1.9	2009	66
20.2	1.8	1854	51
23	1.6	1794	38
25.4	1.5	1857	45
25.6	1.5	1868	36
32.2	1.3	1793	42
37.5	1.1	1751	20

Table 11. ^{9}Li cross sections on tantalum.

Energy MeV u^{-1}	*Error* MeV u^{-1}	*Cross Section* mb	*Error* mb
18.8	1.1	3730	354
20.9	1	4201	132
23.7	0.9	4152	148
26.2	0.9	4224	157
32.7	0.7	4131	134
33.1	0.3	4426	100

Table 12. ^{9}Li cross sections on cobalt.

Energy MeV u^{-1}	*Error* MeV u^{-1}	*Cross Section* mb	*Error* mb
19.4	0.5	1848	154
21.5	0.4	2203	64
26.7	0.4	2715	85
33.1	0.3	2089	110

Table 13. ^{10}Be cross sections on silicon.

Energy MeV u^{-1}	*Error* MeV u^{-1}	*Cross Section* mb	*Error* mb
34.4	0.6	1668	55
37.5	1.8	1710	43
40.5	1.7	1675	38
48.6	1.5	1678	54

Table 14. ^{10}Be cross sections on tantalum.

Energy MeV u^{-1}	*Error* MeV u^{-1}	*Cross Section* mb	*Error* mb
35.1	0.4	3842	139
38.3	1.1	3866	160
41.2	1	4131	174
49.2	0.9	4201	174
49.7	0.4	4376	140

Table 15. ^{10}Be cross sections on cobalt.

Energy MeV u^{-1}	*Error* MeV u^{-1}	*Cross Section* mb	*Error* mb
35.8	0.2	1806	63
41.8	0.4	2338	88
49.7	0.4	2068	155

Table 16. ^{11}Be cross sections on silicon.

Energy MeV u^{-1}	*Error* MeV u^{-1}	*Cross Section* mb	*Error* mb
17.9	2.8	2417	296
22.3	2.4	2233	44
26.4	2.1	2152	33
28.7	2	2320	180
29.8	1.9	2226	31
39.4	1.6	2103	34
45.4	1.4	2008	75

Table 17. ^{11}Be cross sections on tantalum.

Energy MeV u^{-1}	*Error* MeV u^{-1}	*Cross Section* mb	*Error* mb
23.3	1.4	4738	259
27.3	1.2	4614	121
30.6	1.1	4863	132
39.5	0.9	4865	111
40	0.4	5247	116

Table 18. ^{11}Be cross sections on cobalt.

Energy MeV u^{-1}	*Error* MeV u^{-1}	*Cross Section* mb	*Error* mb
20	0.7	3960	935
24.1	0.6	2775	66
31.3	0.5	2764	67
40	0.4	2371	86

Table 19. ^{12}Be cross sections on silicon.

Energy MeV u^{-1}	*Error* MeV u^{-1}	*Cross Section* mb	*Error* mb
10	3.7	3512	179
16.1	2.8	2669	105
17	2.7	2230	192
20.8	2.3	2592	95
31.3	1.7	2223	77
37.2	1.5	2023	60

Table 20. ^{12}Be cross sections on tantalum.

Energy MeV u^{-1}	*Error* MeV u^{-1}	*Cross Section* mb	*Error* mb
11.8	1.9	8606	1548
17.4	1.5	6944	436
21.8	1.3	6887	443
32	1	5852	274
32.5	0.4	6158	333

Table 21. ^{12}Be cross sections on cobalt.

Energy MeV u^{-1}	*Error* MeV u^{-1}	*Cross Section* mb	*Error* mb
12.8	0.9	3670	303
22.5	0.6	2975	195
32.5	0.4	2957	197

Table 22. ^{14}B cross sections on silicon.

Energy MeV u^{-1}	*Error* MeV u^{-1}	*Cross Section* mb	*Error* mb
22.3	2.9	2179	101
35.9	2.1	2584	98

Table 23. ^{14}B cross sections on tantalum.

Energy MeV u^{-1}	*Error* MeV u^{-1}	*Cross Section* mb	*Error* mb
23.5	1.6	6023	484
36.7	1.2	4918	307
36.7	1.2	6035	382

Table 24. ^{14}B cross sections on cobalt.

Energy MeV u^{-1}	*Error* MeV u^{-1}	*Cross Section* mb	*Error* mb
24.4	0.7	3132	233
37.4	0.5	3468	255

D Extra figures and pictures

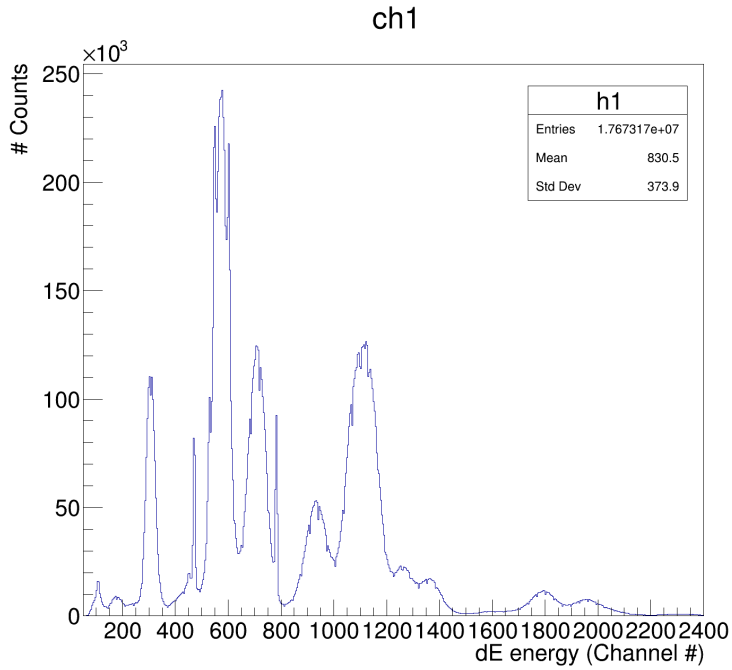

Figure 19. dE spectrum. All isotopes can be seen, but they overlap.

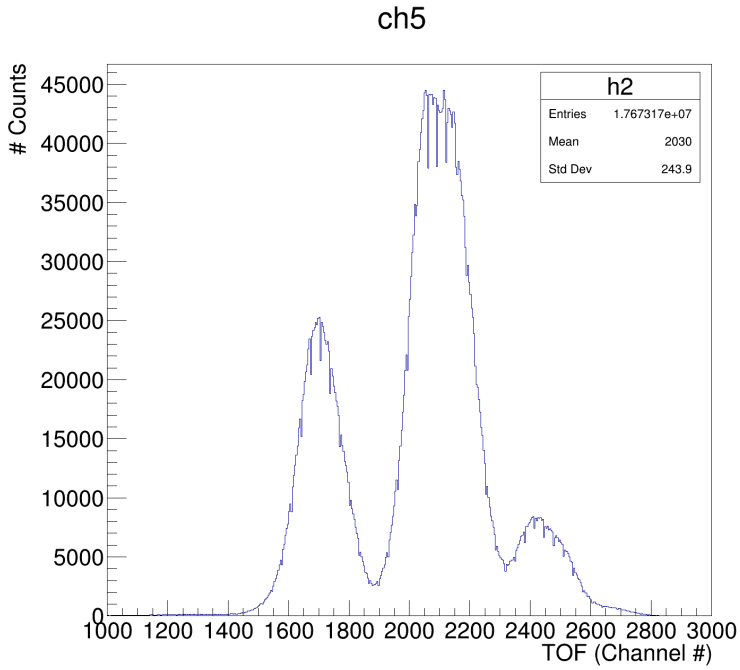

Figure 20. TOF spectrum. Each peak contains all isotopes of an element.

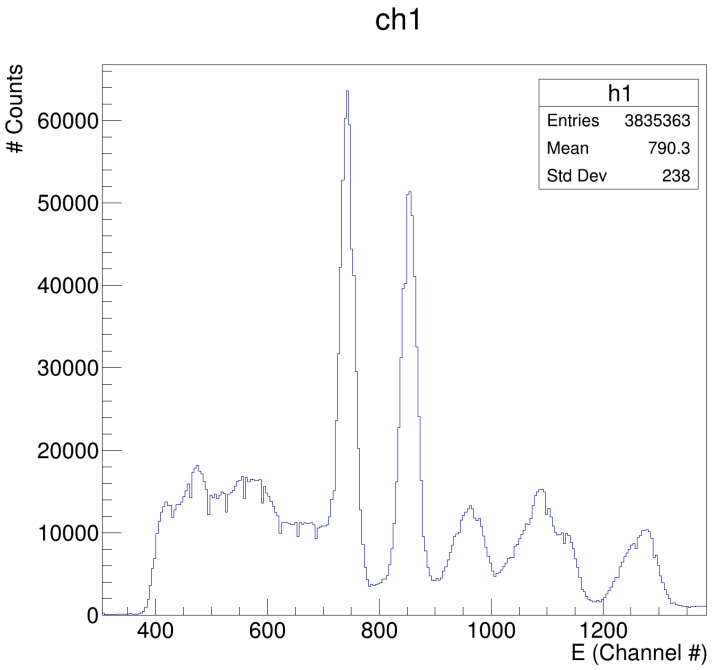

Figure 21. $CeBr_3$ energy spectrum from the ^{60}Co calibration run.

Figure 22. ^{59}Co and Si targets. Silicon target is mounted on the target holder.

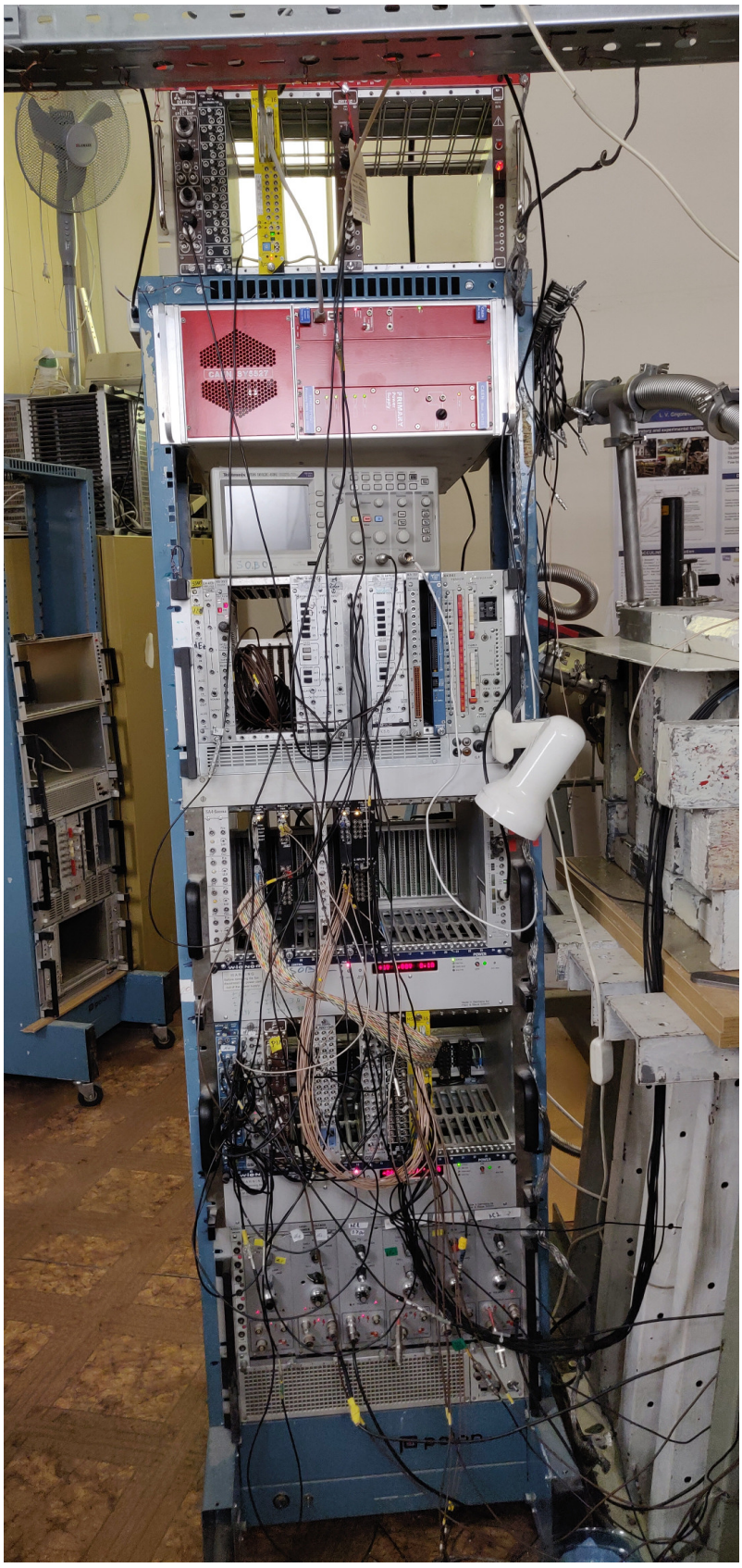

Figure 23. Most of the NIM and CAMAC electronics, used in the experiment.